

Scatter Correction in X-Ray CT by Physics-Inspired Deep Learning

Berk Iskender and Yoram Bresler

Abstract—A fundamental problem in X-ray Computed Tomography (CT) is the scatter due to interaction of photons with the imaged object. Unless corrected, scatter manifests itself as degradations in the reconstructions in the form of various artifacts. Scatter correction is therefore critical for reconstruction quality. Scatter correction methods can be divided into two categories: hardware-based; and software-based. Despite success in specific settings, hardware-based methods require modification in the hardware, or increase in the scan time or dose. This makes software-based methods attractive. In this context, Monte-Carlo based scatter estimation, analytical-numerical, and kernel-based methods were developed. Furthermore, data-driven approaches to tackle this problem were recently demonstrated. In this work, two novel physics-inspired deep-learning-based methods, PhLSCAT and OV-PhLSCAT, are proposed. The methods estimate and correct for the scatter in the acquired projection measurements. They incorporate both an initial reconstruction of the object of interest and the scatter-corrupted measurements related to it. They use a common deep neural network architecture and cost function, both tailored to the problem. Numerical experiments with data obtained by Monte-Carlo simulations of the imaging of phantoms reveal significant improvement over a recent purely projection-domain deep neural network scatter correction method.

Index Terms—Scatter correction, Computed tomography (CT), Deep learning, neural network, CNN, Monte-Carlo, parallel beam, cone beam.

I. INTRODUCTION

The contrast in X-ray transmission computed tomography (CT) is based on materials absorbing photons differently according to their electron densities [1]. Transmission measurements obtained from different view angles are processed to obtain cross-sectional (tomographic) images of the object of interest. CT used widely for imaging internal structures of the body and for non-destructive evaluation [2].

In X-ray CT, scatter occurring due to the interaction of radiation with objects degrades the reconstruction by causing streaks, cupping, shading artifacts and decrease in contrast. These severe artifacts due to scatter make its prevention or

correction one of the major steps to preserve the reconstruction quality in CT.

De-scattering methods fall into two main categories: hardware-based; and software-based. Hardware-based methods include collimation, introducing a bow-tie filter in front of the X-ray source, increasing the distance between the detector and scattering object, use of an anti-scatter grid, etc. [3]. These methods are successful in particular settings. However, they are either costly to implement or they subject the patient to a greater X-ray dose, which may pose a health risk.

In this regard, software-based scatter estimation and correction methods are preferable since they avoid modification in the data acquisition process. These methods, in turn, fall into two classes: (i) methods that estimate the scatter for a given object and imaging scenario using a forward solver; and (ii) methods that work directly on the total projection data. We consider Class (i) first, and the forward solvers that it uses.

Given a specification of an object, X-ray source, and imaging geometry, the forward problem in scatter modeling is to compute the expected value s of the scatter incident on the detector. One of the main approaches to model scatter in X-ray CT is Monte-Carlo (MC)-based. MC forward solvers, which rely on the classical Monte-Carlo integration theory, stochastically sample photon propagation to estimate the scatter for a given object. For a given object, MC forward solver-based correction methods [4] can estimate the scatter component quite accurately. However, to obtain accurate estimates, the MC technique requires numerous photons, leading to a trade-off between stochastic noise in the estimates and runtimes. Therefore, despite their potential to produce gold standard estimates of scatter, the computational costs and runtimes of MC-based methods are prohibitive for clinical purposes.

Unlike the MC stochastic modeling of scatter, the linear Boltzmann transport equation (LBTE) specifies a solution for the expected value of the scatter. To mitigate the computational cost of solving the LBTE, which is an integro-differential equation in a seven dimensional space, analytical-numerical forward solvers use simplifying assumptions to find an approximate solution [5], [6]. Although faster than MC, this approach involves a trade-off between numerical discretization and the maximum order of scatter that is modeled, and the accuracy of the scatter estimate, therefore it too can be computationally expensive.

The third method for the forward problem is the slice-by-slice method [7], which models the scatter as a distance-dependent incremental blurring effect represented by kernels. This method only models the first-order Compton scatter,

This work was supported in part by the National Science Foundation (NSF) under Grant IIS 14-47879, by US Army MURI Award W911NF-15-1-0479, and by a Los Alamos National Labs Contract No. 599416.

Berk Iskender and Yoram Bresler are with the Department of Electrical and Computer Engineering, and the Coordinated Science Laboratory, University of Illinois at Urbana-Champaign, Urbana, IL 61801 USA. (e-mail: berki2@illinois.edu; ybresler@illinois.edu)

relying on its dominance in X-ray CT [2], and uses the Klein-Nishina formula [8] to obtain the kernels. This method has a reduced computational cost compared to the first two. However, it is unable to keep track of the angular distributions of the incoming photons to a slice and does not account for any multiple order scattering events in the medium, which limit its effectiveness.

In contrast to the forward-solver based methods, the Class (ii) methods work directly on the total, scatter corrupted projection data. They can be further classified, in turn, into two categories: kernel-based scatter estimation; or data-driven scatter estimation in the projection domain.

Given scatter-corrupted total measurements $\tau(t, \theta)$, kernel-based scatter estimation methods attempt to determine the scatter in $\tau(t, \theta)$ by convolving its weighted version $\tilde{\tau}(t, \theta)$ with a specific function of t - a "kernel" [9]–[11] for each view θ . These estimation methods are computationally efficient but prior assumptions such as neglecting the contribution of scatter to the total measurement and pre-defined kernels with few degrees of freedom restrict their effectiveness.

Instead, data-driven approaches in the projection domain utilize neural networks to estimate scatter from given total scatter-corrupted measurements. Recent work includes a correction method for Cone Beam CT (CBCT) with two-step registration (CT-CBCT pairs) [12]; a CBCT method using a scatter library of breast CT to estimate scatter [13]; and a two-network approach that learns scatter by separating it into high and low frequency components [14]. A data-driven method called Deep Scatter Estimation (DSE in short) [15], [16], operates on the projection domain and uses a modified U-net [17] architecture with an additional average pooling path for better extraction of features. However, these methods use little or no information of the 3D object structure, which ultimately determines the scatter, thus limiting their effectiveness. The DSE method serves as a benchmark in our work and its results are compared with the results of our proposed methods.

In this work¹, unlike previous Deep Neural Network (DNN)-based approaches, we present scatter correction algorithms for X-ray CT based on a deep CNN that use both the raw projection data and an initial reconstructed image simultaneously. The data processing pipelines, network architectures, and loss function design for training of the proposed methods are all inspired by the physics of X-ray scatter. The specific loss function also makes it possible to express the norm of a reconstruction domain error in the projection domain, avoiding the need to compute gradients (backpropagate) across the filtered backprojection algorithm for every training sample, resulting in efficient network training. This loss function may therefore be of independent interest in other work on deep-learning methods in tomography.

The organization of the work is as follows. In Section II, the fundamentals of the computed tomography, the physics of scatter, and existing scatter correction methods are reviewed. The proposed algorithms are described in detail in Section III. The methodology and framework for the numerical experiments

¹See also [18], [19] for a condensed presentation of a 2D version of our approach, with results restricted to the parallel-beam geometry and a monochromatic source.

are provided in Section IV. The performance of the proposed methods and the results of the various numerical experiments are presented in Section V. We conclude in Section VI and indicate possible future directions for research.

II. X-RAY COMPUTED TOMOGRAPHY AND SCATTER

A. X-Ray CT

In X-ray CT, measurements of the attenuation of X-rays as they pass through the object are used to derive line integral measurements of the distribution of the linear attenuation coefficient in the object. In a 2D setting with a parallel beam source, shown in Fig. 1, let f denote the object (i.e., the desired image) with $f(\mathbf{x})$ the linear attenuation coefficient at position $\mathbf{x} \in \mathbb{R}^2$. The line integral of f along the ray parametrized by offset (detector position) t and angle θ is denoted by $g(t, \theta)$. For fixed θ , the function $g(\cdot, \theta)$ is called a projection of f at view angle θ , and the mapping from f to the complete set of line integral projections $g \triangleq \{g(t, \theta), \theta \in [0, \pi), t \in \mathbb{R}\}$ is the 2D Radon transform, a linear operator denoted by \mathcal{R} ,

$$g(t, \theta) = (\mathcal{R}f)(t, \theta). \quad (1)$$

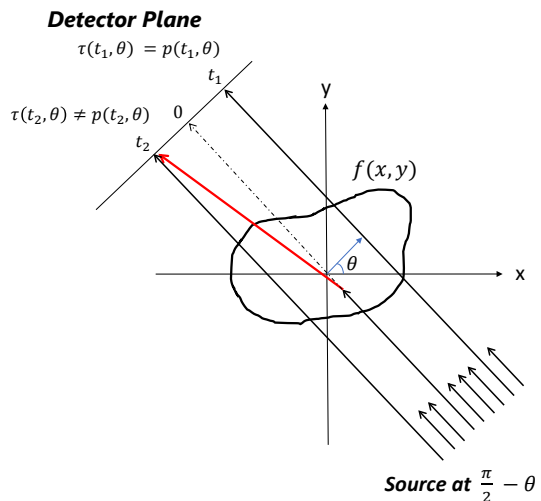


Fig. 1: 2D parallel-beam CT geometry, and x-ray scatter. An x-ray directed toward the detector position $(0, \theta)$ reaches the detector at (t_2, θ) after scattering in the object f , causing $\tau(t_2, \theta) \neq p(t_2, \theta)$.

The tomographic reconstruction problem is to compute the inverse Radon transform $f(\mathbf{x}) = (\mathcal{R}^{-1}g)(\mathbf{x})$. An analytical solution is provided by Filtered Back Projection (FBP) [1].

In practice, projections are measured only at a finite set of view angles, $\theta \in \Theta$ (typically $\Theta = \{2k\pi/K, k = 0, 1, \dots, K-1\}$), and at a finite set of ray offsets $T \triangleq \{t = i\Delta_t, i = -(d-1)/2, \dots, 0, \dots, (d-1)/2\}$ per view, resulting in a discrete set of projections, $g \triangleq \{g(t, \theta), \theta \in \Theta, t \in T\}$.

We use $\mathbf{g}_\theta \in \mathbb{R}^d$ to denote the discrete projection at angle θ - the vector of d uniformly-spaced samples of $g(t, \theta)$ along the detector position coordinate, t .

To obtain a unique solution in the discrete case, f is restricted to some special subspace or set. With the usual

assumption that f is essentially bandlimited and supported on a bounded set, and the sampling in θ and t dense enough [1], the discrete-index FBP is a good numerical approximation to the inverse of the Radon transform. We denote the FBP by $\widehat{\mathcal{R}^{-1}}$, to emphasize that we assume that the conditions for accurate reconstruction by FBP are satisfied, and focus on the error due to scatter.

We turn now to the important step of computing the line integral values from the X-ray detector measurements. The attenuation of an X-ray beam depends on the energy of its photons and on the object along its propagation path. The two types of sources in X-ray imaging are polychromatic, emitting photons with a broad range of energies, and monochromatic, emitting essentially monoenergetic rays. Polychromatic X-ray sources, such as X-ray tubes, are the more common, whereas monochromatic sources arise mostly in synchrotron imaging, which has important applications [20]–[23], and is now becoming available in compact source implementations [24], [25]. Synchrotron imaging is well-modeled by the parallel-beam imaging geometry, so that the methods developed in this paper for this geometry are directly applicable to it.

In our analysis, we assume a two-dimensional object f illuminated by a parallel beam source. The fraction of attenuated photons per unit thickness of the object at each energy level is described by the energy-dependent linear attenuation coefficient [26] $f_E(\mathbf{x})$ of the object at position $\mathbf{x} \in \mathbb{R}^2$ for source energy E . Then, the line-integral of f_E at angle $\theta \in [0, 2\pi)$, detector position $t \in \mathbb{R}$, and source energy E can be written as

$$g_E(t, \theta) = (\mathcal{R}f_E)(t, \theta). \quad (2)$$

Using an energy-integrating detector, the *primary measurement* at position t at angle θ is, by Beer's law [27],

$$p(t, \theta) = I_0 \int c(E) e^{-g_E(t, \theta)} dE, \quad (3)$$

where I_0 is the vacuum (or bright field) fluence measurement, $c(E)$ denotes the fraction of source photon fluence scaled by the energy-dependent detector response at energy E , and where $\int c(E) dE = 1$, and $f_E(\mathbf{x})$ is the linear attenuation coefficient at energy E and at position \mathbf{x} .

With a monochromatic source with photon energy E_0 , (2) reduces to (1) and (3) reduces to

$$p(t, \theta) = I_0 e^{-g(t, \theta)}, \quad (4)$$

where the dependence on E_0 is suppressed to simplify notation. In this case, the line integral projection is readily extracted from the measurement by a logarithm, $g(t, \theta) = -\ln[p(t, \theta)/I_0]$.

On the other hand, in the polychromatic case, it is evident from (3) that the mapping from g_E to the primary measurements p involves another nonlinearity in addition to the exponential, which cannot be inverted by taking the logarithm. Depending on the material composition of the object, this nonlinearity, unless corrected, may manifest as so-called beam hardening artifacts in the reconstruction. To focus on scatter correction only, we limit the discussion in the remainder of this section and in Secs. III–IV to the monochromatic

case. However, the general approach can be extended to the polychromatic setting to handle scatter and beam hardening simultaneously. This is demonstrated in the numerical experiments in Section V.

Given the primary measurements p , the projections g determined by inverting (4) should suffice to obtain an accurate reconstruction by FBP. However, as discussed next, due to X-ray scatter, the primary measurements are corrupted by an additive scatter component, which unless blocked in the first place by physical means, or corrected, result in artifacts in the reconstruction.

While any practical CT measurements also include random noise due to finite number of photons and electronic noise at the detector, in our discussion we assume sufficient photon counts and sufficiently small electronic noise in the measurements that the reconstruction error is dominated by the deterministic bias due to scatter, rather than by the variance due to noise.

B. X-Ray Scatter

X-rays can undergo several types of interactions as they propagate through matter. Considering the medical CT energy range, which goes up to 140 keV and non-destructive tomography (NDT) using X-ray tubes, whose energy range is up to 450 keV, the interactions that play a role are Rayleigh (coherent) scattering, Compton (incoherent) scattering and the photoelectric effect. Of these, Rayleigh scatter is significant only up to 30 keV, and the photoelectric effect has negligible contribution to the detected scatter signal because the secondary X-rays emitted have low energy and are mostly absorbed by the imaged object [28]. The only significant source of scatter at X-ray energies of 30 keV - 450 keV is therefore Compton scatter. Our discussion will therefore focus on this effect.

Compton scattering is the scattering of an incident photon by a charged particle, usually an electron. The probability of observing Compton scattering increases with the energy of the photons. Part of the energy of the photon is transmitted to the electron, and the propagation direction of the photon and its energy are both modified, usually by a non-negligible amount. This is illustrated in Fig. 1, where an X-ray at direction θ propagating toward detector position $t = 0$ reaches instead the detector at position $t = t_2$ after scattering in the object f . With many such scattering events, the *total measurement* (detector reading) at angle θ that is obtained is

$$\tau(t, \theta) = p(t, \theta) + s(t, \theta), \quad (5)$$

where $s(t, \theta)$ is an additive *scatter term*, which is a nonlinear function of the object.

It is the contribution of this additive term that leads to artifacts in conventional reconstruction where FBP is directly implemented using the total, scatter corrupted, measurement τ instead of the ideal primary measurement p to obtain an estimate $f^* \in \mathbb{R}^{d^2}$ of the image.

C. Problem Statement

We assume that we are given a set total measurements $\tau \triangleq \{\tau_\theta, \theta \in \Theta\}$ which, in the absence of the scatter

component s , would suffice for accurate reconstruction of the object f by FBP. Our goal is to produce a reconstruction f^* that approximates the FBP reconstruction $\hat{f} = \widehat{\mathcal{R}^{-1}g}$ that would be obtained from $g(t, \theta) = -\ln[p(t, \theta)/I_0]$, where p is the, scatter-free, set of primary measurements.

III. SCATTER CORRECTION BY PHYSICS-INSPIRED ALGORITHMS

To make the proposed methods applicable for various vacuum (air) fluences without change, the problem and method are formulated in terms of the normalized quantities, $\bar{\tau}_\theta \triangleq \tau_\theta/I_0$, $\bar{s}_\theta \triangleq s_\theta/I_0$, and $\bar{p}_\theta \triangleq p_\theta/I_0$. We denote the set of normalized total measurements by $\bar{\tau} \triangleq \{\bar{\tau}_\theta, \theta \in \Theta\}$, with $\bar{\tau}_\theta \in \mathbb{R}^d$. Given $\bar{\tau}$, the problem is to produce an estimate \bar{p}^* of the scatter-free primary, which is then used to reconstruct the estimate f^* using FBP.

A. PhilSCAT: Physics-Inspired Learned Scatter Correction Algorithm [18]

A block diagram of the algorithm is presented in Fig. 2. The key idea in the proposed approach, is that because scatter in any one direction depends on the entire object in a nonlinear fashion, the measurement in one direction cannot be used to fully determine the scatter in that direction. Instead, information about the entire object is required. Thus, given a set of normalized total measurements, $\bar{\tau}$, an initial reconstruction estimate $\tilde{f} \in \mathbb{R}^{d^2}$ of the image is computed by FBP

$$\tilde{f}(\mathbf{x}) = (\widehat{\mathcal{R}^{-1}\tilde{g}})(\mathbf{x}), \quad (6)$$

where

$$\tilde{g}(t, \theta) = -\ln \min\{\bar{\tau}(t, \theta), 1\} \quad (7)$$

is an initial estimate of the line integral projection. To obtain the initial reconstruction in (6)-(7), $\tau(t, \theta)$ is used as a surrogate for the primary measurement $p(t, \theta)$. By the inherent physics in (3) or (4), $p(t, \theta)$ must be smaller than the mean bright field fluence I_0 . Hence, this physical constraint is used in (7) to improve the initial reconstruction, by clipping of $\bar{\tau}(t, \theta)$ to 1, or equivalently clipping of $\tau(t, \theta)$ to I_0 .

The deep convolutional neural network (DCNN), \mathcal{N}_γ with network parameters γ , operates view-by-view. It accepts two different inputs:

- (i) a normalized post-log total measurement $-\ln \bar{\tau}_\theta$ at view angle θ . Here, unlike (7), the normalized total measurement $\bar{\tau}_\theta$ at the input to the DCNN is not upper bounded by 1, because values greater than 1 are physically possible after the normalization by I_0 and they provide useful information for the estimation of the normalized scatter term \bar{s}_θ .
- (ii) a version $\tilde{f}_\theta \in \mathbb{R}^{d^2}$ of the initial reconstruction estimate that is rotated by the same angle θ of the projection being processed. As a consequence of the rotation, a projection of \tilde{f}_θ at zero angle yields the projection of \tilde{f} at angle θ , allowing the DCNN to be agnostic to θ .

The DCNN returns an estimate $\bar{s}_\theta^* \in \mathbb{R}^d$ of the scatter component

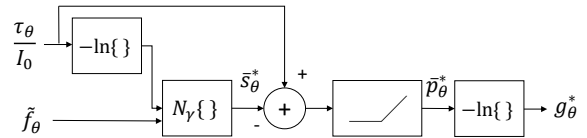


Fig. 2: Block diagram of PhilSCAT.

$$\bar{s}_\theta^* = \mathcal{N}_\gamma \left(\tilde{f}_\theta, -\ln \bar{\tau}_\theta \right). \quad (8)$$

The normalized primary measurement is ultimately estimated as

$$\bar{p}_\theta^* = \max\{\bar{\tau}_\theta - \bar{s}_\theta^*, 0\}. \quad (9)$$

The clipping of \bar{p}^* is again due to the physical constraint imposed by (3) or (4). Finally, an estimate g_θ^* of the projection is obtained as $g^*(t, \theta) = -\ln(\bar{p}^*(t, \theta))$. Once every view has been processed by the algorithm, the reconstructed image is obtained from g^* by FBP with Shepp-Logan filtering [29],

$$f^*(\mathbf{x}) = (\widehat{\mathcal{R}^{-1}g^*})(\mathbf{x}). \quad (10)$$

The steps of the algorithm are listed as Algorithm 1.

Algorithm 1 PhilSCAT

Input: $\{\bar{\tau}_\theta = (\tau_\theta/I_0) \in \mathbb{R}^d, \theta \in \Theta\}$

Output: $f^*(\mathbf{x})$

1. Initial Reconstruction:

for $\theta \in \Theta$ **do**

$$\tilde{g}(t, \theta) = -\ln \min\{\bar{\tau}(t, \theta), 1\}$$

end for

$$\tilde{f} = (\widehat{\mathcal{R}^{-1}\tilde{g}})(\mathbf{x}) \in \mathbb{R}^{d^2}$$

2. Scatter and Primary Estimation:

for $\theta \in \Theta$ **do**

Rotate \tilde{f} by angle θ , obtain \tilde{f}_θ

$$\bar{s}_\theta^* = \mathcal{N}_\gamma(\tilde{f}_\theta, -\ln \bar{\tau}_\theta)$$

$$\bar{p}_\theta^* = \max\{\bar{\tau}_\theta - \bar{s}_\theta^*, 0\}$$

end for

$$g_\theta^* = \max\{-\ln \bar{p}_\theta^*, 0\}$$

3. Final Reconstruction:

$$f^*(\mathbf{x}) = (\widehat{\mathcal{R}^{-1}g^*})(\mathbf{x})$$

B. OV-PhilSCAT: Opposite-View processing PhilSCAT [19]

This algorithm is a variation on PhilSCAT, utilizing one more physical aspect of the tomographic measurement. We take advantage of the following property of the 2D Radon transform: the line integral projections in opposite directions coincide up to a sign reversal (flip) in t : $g(t, \theta) = g(-t, \theta + \pi)$. We call such a pair of projections π -opposite projections, and denote the t -flipped version of g_θ by \hat{g}_θ . Combining this with (3) and (4) we have

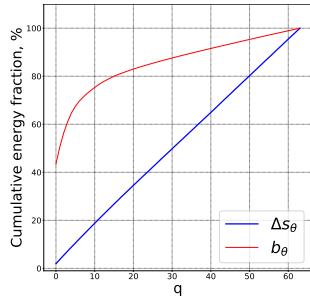


Fig. 3: Cumulative fraction of the total energy contained in the frequency components $[0, q]$.

$$\begin{aligned} g_\theta &= \hat{g}_{\theta+\pi}, \\ \bar{p}_\theta &= \hat{\bar{p}}_{\theta+\pi}, \\ \bar{\tau}_\theta - \hat{\tau}_{\theta+\pi} &= \bar{s}_\theta - \hat{s}_{\theta+\pi} \triangleq \Delta\bar{s}_\theta. \end{aligned} \quad (11)$$

It follows that the difference $\Delta\bar{s}_\theta$ of π -opposite scatter components can be determined *exactly* from the available (scatter-corrupted) total measurements. Thus, estimating the average $\bar{b}_\theta \triangleq (\bar{s}_\theta + \hat{s}_{\theta+\pi})/2$ suffices to fully determine the individual scatter components. This approach is motivated by the following hypothesis:

H1 estimating the average \bar{b}_θ should be easier than estimating \bar{s}_θ and $\hat{s}_{\theta+\pi}$ on their own, because \bar{b}_θ is typically smoother than \bar{s}_θ , and therefore \bar{b}_θ should be easier to learn by a deep neural network.

In contrast, the difference $\Delta\bar{s}_\theta$ typically has higher bandwidth, however, we do not need to estimate it, since it can be extracted exactly from the total measurements (the measured data).

The smoothness of \bar{b}_θ relative to $\Delta\bar{s}_\theta$ can be observed in Fig. 3. To obtain this figure, we first computed estimates of the power spectra $S_\Delta[i]$ and $S_b[i]$, $i = 0, 1, \dots, 63$, of Δs_θ and b_θ , respectively, by taking the squared magnitude discrete Fourier transform (DFT) of $\Delta s_\theta(t)$ and $b_\theta(t)$ with respect to detector coordinate t discretized to 64 pixels, and then averaging over 360 view angles $\theta \in \Theta$, and over 27 different phantoms. The phantoms used to compute these estimates were drawn from the 3D monochromatic parallel beam experiments, described in Section IV-A. Then, we determined the fraction of energy contained in the frequencies up to $q \in \{0, \dots, Q-1\}$ by computing the cumulative sums $\sum_{i=0}^q S_\Delta[i]$ and $\sum_{i=0}^q S_b[i]$ and normalizing by the respective total energies.

As seen in Fig. 3, Δs_θ has a power spectrum close to that of white noise, with cumulative energy fraction increasing linearly with frequency. In contrast, b_θ has a large fraction of its energy concentrated in the first few frequency components: the DC component alone accounts for about 45%, and the first 11 components capture about 75% of the energy in b_θ .

Given b_θ , then, using the relation between the π -opposite primaries, it follows that

$$\bar{p}_\theta = \frac{\bar{\tau}_\theta + \hat{\tau}_{\theta+\pi}}{2} - \bar{b}_\theta. \quad (12)$$

In view of the foregoing observations, OV-PhILSCAT operates on averages $(\bar{\tau}_\theta + \bar{\tau}_{\theta+\pi})/2$ of normalized π -opposite

total projections, and outputs estimates of the average \bar{b}_θ of normalized π -opposite scatter, and of the primary \bar{p}_θ .

The DCNN \mathcal{N}_γ , also operates view-by-view but instead of K times, as in PhILSCAT, it is used here $K/2$ times, for $\theta = k(2\pi/K)$, $k = 0, 1, \dots, K/2 - 1$. This computational improvement is obtained by using the equivalence of π -opposite projections.

The network takes two inputs:

- (i) the average $(\bar{\tau}_\theta + \hat{\tau}_{\theta+\pi})/2$ of normalized pre-log π -opposite total measurements at view angle θ ,
- (ii) the initial reconstruction estimate rotated by θ , $\tilde{f}_\theta \in \mathbb{R}^{d^2}$. Different than PhILSCAT, \tilde{f} is obtained by using $(\bar{\tau}_\theta + \hat{\tau}_{\theta+\pi})/2$ for $\theta = k(2\pi/K)$, $k = 0, 1, \dots, K/2 - 1$.

The DCNN produces an estimate of the average $\bar{b}_\theta^* \in \mathbb{R}^d$ of the normalized π -opposite scatter components

$$\bar{b}_\theta^* = \mathcal{N}_\gamma \left(\tilde{f}_\theta, -\ln \frac{\bar{\tau}_\theta + \hat{\tau}_{\theta+\pi}}{2} \right). \quad (13)$$

The normalized primary projection \bar{p}_θ is then estimated as

$$\bar{p}_\theta^* = \max \left\{ \frac{\bar{\tau}_\theta + \hat{\tau}_{\theta+\pi}}{2} - \bar{b}_\theta^*, 0 \right\}, \quad (14)$$

and, as in Section III-A to reflect the physical constraints, we constrain \bar{p}_θ to be non-negative. Similarly, $\bar{\tau}_\theta$ is not clipped to 1, since $\bar{\tau}_\theta > 1$ is physically possible.

Finally, the reconstruction estimate is obtained using FBP with Shepp-Logan filtering [29], as in (10), this time only using estimates of the projection g_θ^* from half of the angular range $\Theta = \{2k\pi/K, k = 0, 1, \dots, K/2 - 1\}$.

C. Loss Function

The networks in both algorithms are trained by minimizing a common loss function with respect to the network parameters γ . In other work [15] on learning-based scatter estimation, the loss function is expressed in terms of the difference $p - p^*$ between the primary measurements and their estimate. However, because the image produced by the FBP algorithm depends logarithmically on p , it is the *relative* error in p^* that matters. Therefore, an error with the same magnitude in p^* has greater impact on the reconstruction f^* for smaller p than for larger p . It follows that measuring the loss in terms of the error p^* would not reflect the error in the reconstructed image, with the effect manifesting most strongly for rays passing through highly attenuating regions.

Instead, because our goal is to approximate the scatter-free FBP reconstruction \hat{f} by f^* , a reasonable choice for a loss function to represent the relevant deviation averaged over M training samples would be

$$L(\gamma) = (1/M) \sum_{m=1}^M \hat{\Lambda}[\hat{f}_m, f_m^*(\gamma)]$$

$$\begin{aligned} \text{where } \hat{\Lambda}[\hat{f}, f^*(\gamma)] &\triangleq \|Q[\hat{f} - f^*(\gamma)]\|_2^2 \\ &= \|\widehat{QR^{-1}}[g - g^*(\gamma)]\|_2^2. \end{aligned} \quad (15)$$

In (15) $g_\theta^*(\gamma) = -\ln \bar{p}_\theta^*(\gamma)$ and $g_\theta = -\ln \bar{p}_\theta$ are the estimated and the true line integral projections of the object, with

the dependence on γ arising from (8)-(9) for PhILSCAT, or (13)-(14) for OV-PhILSCAT. Operator \mathcal{Q} represents possible perceptual weighting of the reconstruction error in the image domain. In particular, to account for the perceptual significance of edges in CT images, we consider \mathcal{Q} that corresponds to an image-domain filter with radially symmetric high-pass frequency response $Q(\omega)$ (in polar coordinates).

A drawback of the loss function (15) is that to compute its gradients, it requires back-propagation across the FBP operator \mathcal{R}^{-1} for every training sample, which can be computationally expensive. Instead, we show in the next subsection that the loss (15) can be expressed directly and exactly in terms of the projections, without the need for an FBP. This leads to the following modified loss function

$$\Lambda[g, g^*(\gamma)] = \sum_{\theta \in \Theta} \|h * (g_\theta - g_\theta^*)(\gamma)\|_2^2 + \lambda \|g_\theta - g_\theta^*(\gamma)\|_1. \quad (16)$$

The filtered l_2 -norm term is exactly equivalent to the loss in (15). The filter h is the simple two-tap filter with impulse response

$$h[n] = \frac{1}{2}\delta[n+1] - \frac{1}{2}\delta[n-1], \quad (17)$$

resulting in a very efficient implementation of the loss function and its gradients. Since h is a high-pass filter, the l_1 -norm term (with a small constant, $\lambda > 0$) is used to recover the zero frequency component of the projections. The specific choice of filter h is explained in detail next.

D. Image 2-Norm in Projection Space

In this subsection we derive a simple expression for the reconstruction error in image space, in terms of the error in projection space. This enables to express the image-domain loss for training the neural network in terms of the estimated projections, and to obtain the gradients needed for training while avoiding the need to back-propagate across the FBP. The result in this subsection may therefore be of independent interest for other applications of deep learning in tomography.

Assuming $f \in L_2(\mathbb{R}^2)$ is a finite energy image having line integral projection at angle θ denoted by $g(t, \theta)$, let $G(\omega, \theta)$ denote the one-dimensional Fourier transform of $g(t, \theta)$ with respect to the first variable. Then by Parseval's relation for the Radon transform [1], the 2-norm of the image f is expressed in terms its line integral projections $\{g(t, \theta), -\infty < t < \infty, \theta \in [0, \pi]\}$ by

$$\|f\|_2^2 = \frac{1}{4\pi^2} \int_0^\pi \int_{-\infty}^\infty |G(\omega, \theta)|^2 |\omega| d\omega d\theta. \quad (18)$$

Note that although the inverse Radon transform to compute f from g involves applying the ramp filter $|\omega|$ to the Fourier transform $G(\omega, \theta)$ of the projections, Parseval's relation in (18) involves applying the same ramp filter to the *square* of $|G(\omega, \theta)|$ instead.

Now, we wish to express the 2-norm of an image \hat{f} , obtained from the projections by FBP using a weighted ramp filter $W(\omega)|\omega|$. Because the only difference to the inverse Radon transform is in the additional weight $W(\omega)$ included with the ramp filter to filter $G(\omega, \theta)$, it follows that $\|\hat{f}\|_2^2$ is

given by replacing $G(\omega, \theta)$ in (18) by its weighted version $W(\omega)G(\omega, \theta)$. Finally, incorporating the perceptual filter Q with radially symmetric frequency response in the image domain, is equivalent, by the Radon convolution Theorem [1] to filtering the projections $G(\omega, \theta)$ by the filter with frequency response $Q(\omega)$. It therefore follows that

$$\|\mathcal{Q}\hat{f}\|_2^2 = \frac{1}{4\pi^2} \int_0^\pi \int_{-\infty}^\infty |W(\omega)Q(\omega)G(\omega, \theta)|^2 |\omega| d\omega d\theta \quad (19)$$

In order to obtain an expression in terms of filtered projections, (19) can be rewritten as

$$\|\mathcal{Q}\hat{f}\|_2^2 = \frac{1}{4\pi^2} \int_0^\pi d\theta \int_{-\infty}^\infty |G(\omega, \theta)H(\omega)|^2 d\omega, \quad (20)$$

where

$$H(\omega) = Q(\omega)W(\omega)|\omega|^{\frac{1}{2}} e^{j\phi(\omega)} \quad (21)$$

can be considered as the frequency response of a filter. The phase of H has no effect on the result owing to the absolute value in (20). Thus, it can be chosen arbitrarily - for example as identically zero. Using the standard Parseval's identity for the second integral in (20), the filtering implied by (20) can be expressed and implemented as

$$\|\mathcal{Q}\hat{f}\|_2^2 = \frac{1}{2\pi} \int_0^\pi d\theta \int_{-\infty}^\infty |\hat{u}(t, \theta)|^2 dt, \quad (22)$$

with

$$\hat{u}(t, \theta) = h(t) * g(t, \theta), \quad (23)$$

where $h(t)$ is a filter with frequency response $H(\omega)$ and $*$ denotes convolution in the t variable.

The implication of these results is that a loss function defined in terms of a Q -weighted L_2 error of an image reconstructed using FBP with ramp filter weighting $W(\omega)$, can be expressed in terms of a loss function defined on the projections, using (22) - (23).

For practical implementation, we derive next the discretized version of (22) - (23). When f has bounded spatial support and W is bandlimited such that the reconstruction \hat{f} is bandlimited, and P uniformly spaced view angles over the interval $[0, 2\pi]$ are used, (19)-(23) can be replaced by their discrete analogues

$$\begin{aligned} \|\mathcal{Q}\hat{f}\|_2^2 &= \frac{1}{2\pi P} \sum_{p=0}^{P-1} \int_{-\pi}^\pi \left| Q_d(\nu)W_d(\nu)G_d\left(\nu, p\frac{2\pi}{P}\right) |\nu|^{0.5} \right|^2 d\nu \\ &= \frac{1}{P} \sum_{p=0}^{P-1} \sum_{n=-\infty}^\infty |\hat{u}_d[n, p]|^2, \end{aligned} \quad (24)$$

where $G_d(\nu, \theta)$ is the DTFT with respect to n of $g_d(n, \theta) \triangleq g(n\Delta_t, \theta)$, $W_d(\nu) = W(\frac{\nu}{\Delta_t})$, $Q_d(\nu) = Q(\frac{\nu}{\Delta_t})$ for $\nu \in [-\pi, \pi]$ and

$$\hat{u}_d[n, p] = \hat{h}_d[n] * g_d(n, p(2\pi/P)), \quad (25)$$

where the convolution is over n and \hat{h}_d is a discrete-time filter with frequency response

$$\hat{H}_d(\nu) = Q_d(\nu)W_d(\nu)|\nu|^{0.5}. \quad (26)$$

Finally, since \hat{f} has a bounded support, (25) can be implemented by FFT, or the integral in (24) can be discretized in frequency ν and, using the symmetry of the DFT of a real sequence replaced by the sum

$$2 \sum_{k=0}^{N/2-1} \left| G_D[k, p] W_d \left(k \frac{2\pi}{N} \right) \right|^2 k, \quad (27)$$

where $G_D[k, p] = G_d(k \frac{2\pi}{N}, p \frac{2\pi}{P})$. Expression (27) gets rid of the inverse FFT computation needed to obtain (25).

Considering the special case of $Q(\omega) = |\omega|^{0.5}$, we obtain $\hat{H}_d(\nu) = W_d(\nu)|\nu|$. However, since we use the magnitude in (24), the phase of \hat{H}_d does not matter, and we may use

$$\hat{H}_d(\nu) = W_d(\nu)\nu. \quad (28)$$

The advantage of this particular filter selection is that it removes the jump discontinuity in the derivative of \hat{H}_d at the origin, and can result in a short filter $\hat{h}_d[n]$. For instance, when $W_d(\nu) = \text{sinc}(\nu)$ is selected, which corresponds to a Shepp-Logan ramp filter [29], we obtain $\hat{H}_d(\nu) = \sin(\nu)$, for which the impulse response

$$\hat{h}_d[n] = \frac{1}{2}\delta[n+1] - \frac{1}{2}\delta[n-1] \quad (29)$$

has only two non-zero values. This enables an easy time-domain implementation of the computation in (24) and (25).

E. Extension to 3D

To apply the algorithms to 3D axial geometries, where the rotation axis z is perpendicular to the cross-sectional (x, y) plane, we stack 2D slices in the case of the parallel beam geometry, and use the Feldkamp algorithm [30] for the 3D cone beam geometry. The same Shepp-Logan ramp filtering is used for the FBP, and the loss function (16) is extended to 3D simply by computing the 2-norms over the respective 2D projections g_θ and g_θ^* . One input of the DNN is now the rotated 3D initial reconstruction $\tilde{f}_\theta \in \mathbb{R}^{d \times d \times d}$, and the second is the 2D log total measurement $-\ln \bar{\tau}_\theta \in \mathbb{R}^{d \times d}$ at one view angle for PhilLSCAT, or the average of π -opposite views for OV-PhilLSCAT, which is only used for the parallel beam geometry.

F. Network Structures

For each view angle, we define three coordinates: the first two (one of which is always the axial z coordinate) define the object plane parallel to the detector plane, and the third perpendicular to it. In the case of the parallel beam geometry, the third coordinate coincides with the direction of photon propagation, and the first two index the planes perpendicular to it. The DCNN in Fig. 4, which operates one view angle θ at a time, has convolutions along the first two input coordinates, and a contracting structure in the third. The network architectures for PhilLSCAT and OV-PhilLSCAT are identical except for the input output pairs as described earlier.

The network takes the initial reconstruction \tilde{f}_θ with $-\ln \bar{\tau}_\theta$ (resp. $-\ln \frac{\bar{\tau}_\theta + \bar{\tau}_{\theta+\pi}}{2}$ for OV-PhilLSCAT) concatenated along the third coordinate as a 3D input, and provides the 2D output s_θ^* (resp. b_θ^* for OV-PhilLSCAT).

This specific structure is inspired by the slice-by-slice approach [7], which divides the object into layers perpendicular of the primary X-ray propagation, and based on the Klein-Nishina formula [8], models scatter by a distance-dependent incremental blurring effect at each layer with pre-specified kernels to obtain the scatter estimate for the next layer. Accordingly, because after rotating the initial reconstruction \tilde{f} by angle θ the columns of the input \tilde{f}_θ correspond to object layers perpendicular to propagation of primary X-rays, the network performs convolutions along the first two coordinates of the input, and contracts along the channel coordinate.

At the m -th step, for $m = 1, \dots, \log_2 d$, the network has a ‘‘ladder’’ of convolutions compressing the input information by diadic factors to a set of outputs with number of channels equal to $\{2^{-m}d, 2^{-(m+1)}d, \dots, 1\}$ using different convolutional layers, and conveys the output of those to the following steps via skip connections, concatenating all intermediate outputs from previous steps that have the same number of channels (e.g. s_{14} is concatenated with every s_{m4} , $m < 4$ and s_4 at the end of the 4th step in the diagram, each having $2^{-4}d$ channels). After concatenation in the $m = 2, 3, \dots$ step, another convolutional layer reduces the number of channels back to $2^{-m}d$.

G. Computational Cost in the Inference Phase

The computation in the DCNN is dominated by the cost of convolutions. For 3D reconstructions, 2D convolutions with filters of size $L \times L$ are used. Assuming $d \times d$ detector panel readouts, filtering in the network requires about $L^2 d$ operations per input and output channel. The total cost of the DCNN can be shown to be bounded by $3L^2 d^4$. The DCNN is used K times - once for each projection. This results in total costs of approximately $3L^2 K d^4$ and $3L^2 K d^4 / 2$ for PhilLSCAT and OV-PhilLSCAT, respectively. The cost of FBP is cd^4 with $c \approx 1$ since it is performed for each slice of the $d \times d \times d$ dimensional phantom. Consequently, the total cost of PhilLSCAT and OV-PhilLSCAT in the 3D case can be bounded by $3L^2 K d^4$ and $3L^2 K d^4 / 2$, respectively.

IV. METHODOLOGY

A. Data Generation and Training

In order to train the algorithms, total measurements τ of objects with known ground-truth primary measurements p are needed. Obtaining such data requires a fully characterized CT device and many different phantoms with known material composition and geometry. In our case, it was impractical to obtain such data. Instead, τ for training, validation, and testing data were generated by MC-based simulations.

For each phantom 2D $d \times d$ detector panel readouts, which we call projection measurements, were simulated at K view angles uniformly spaced in $[0, 2\pi)$, each having P photons. The simulated data was divided into training and test sets phantom-wise, grouping all measurements belonging to a phantom into the same set. The proposed algorithms were trained and tested using the loss function L in (16). The neural networks were implemented in Pytorch [31] and trained using the Adam optimizer [32].

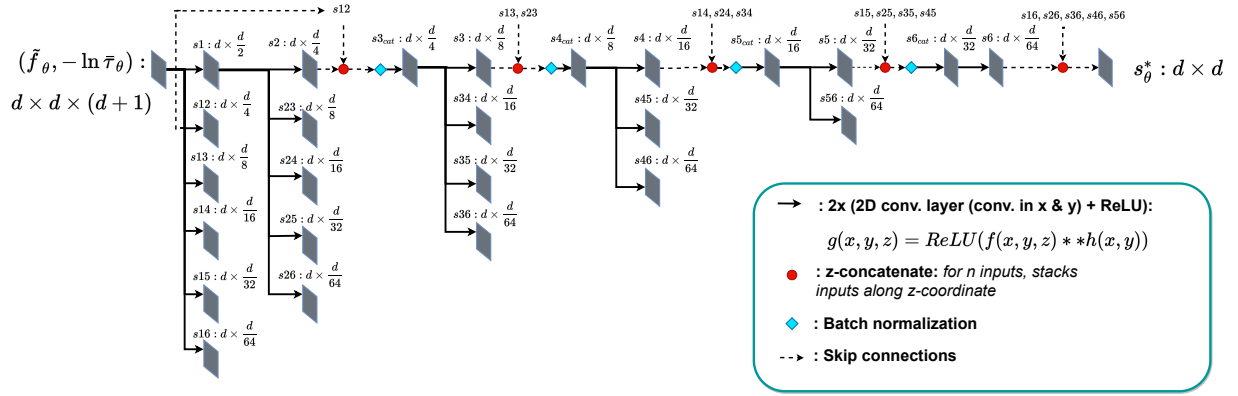


Fig. 4: Proposed network architecture for PhILSCAT for 3D reconstructions.

1) *Parallel Beam CT Experiments*: To obtain the total measurements τ_θ for training and validation for the parallel beam CT experiments, we used the GATE [33] software package. GATE encapsulates the GEANT4 MC [34] simulation libraries, which perform the simulation of particle propagation through matter. On the other hand, the primary projections p_θ of voxelized phantoms were generated by numerical forward projection to compute $g(t, \theta)$ and using Beer’s law (4).

As illustrated in Fig. 5, for these experiments we used a 200 keV monoenergetic parallel-beam source with rays perpendicular to the rotation axis z , and a flat detector panel, both of width $W = 128$ cm and height $H = 128$ cm, with the detector panel perpendicular to the rays of the source, and divided into $(d = 128) \times (d = 128)$ pixels. The source was not collimated, extending over the entire detector. Simulated objects (mathematical phantoms) were generated as a composition of distinct object components, all contained in a cylindrical air volume of diameter $D = 128$ cm and height $L = 128$ cm. The parallel-beam projections of the objects were fully contained in the detector plane for each view, with a margin of approximately 24 cm from the boundaries of the cylindrical geometry in Fig. 5.

The object components in the phantoms were: (i) rectangular prisms; (ii) cylinders with their long axis aligned with the z -axis; and (iii) spheres; with material assigned randomly as water, aluminium, or titanium. Positions and dimensions were randomized, ensuring the components are contained in the phantom volume.

We found in initial experiments that high noise in the simulated training measurements could lead to the networks learning to denoise the projection data rather than just estimating, as intended, the scatter component. This came at the price of reduced resolution of the reconstruction. To mitigate this effect without an expensive increase of the photon counts used in simulation, we introduced a pre-processing step to decrease the level of noise in the simulated measurements.

The idea of the pre-processing step is to identify the areas in the obtained 2D total measurements τ_θ that contain only stochastic noise and little scatter, and smooth them to reduce the noise, without affecting the areas that contain object or significant scatter information. To this end, we used the

analytically calculated primary measurement p_θ corresponding to each projection to determine the areas in the “shadow” of the object using the criterion that these areas only include attenuated fluence $p_\theta < I_0$. These “shadow” regions were used to define an initial binary “smoothing-exclusion mask” $M_\theta \in \{0, 1\}^{d \times d}$, and the non-masked part of the measurements were smoothed to reduce the noise.

To minimize the modification of non-shadow regions containing significant (and informative) scatter by the pre-processing step, we extend the smoothing-exclusion mask to include neighboring out-of-shadow regions. This is motivated by two observations: (i) scatter outside the object shadow is most significant near the shadow boundaries; and (ii) further away from the shadow boundaries the scatter is spatially smooth, and will suffer little change when filtered by the noise-smoothing filter. To this end, each binary smoothing-exclusion mask was modified by morphological dilation with a 5×5 pixel structuring element k , producing the extended smoothing-exclusion mask $\tilde{M}_\theta = k \oplus M_\theta$.

Finally, the regions in the complement of the mask were smoothed by a 2D filter G with Gaussian impulse response with width parameter σ^2 . The smoothed regions were truncated back to the complement of the support of the smoothing-exclusion mask, and combined with the regions in the support of the smoothing-exclusion mask.

A parameter setting of $\lambda = 5 \cdot 10^{-2}$ was used in the loss function L in (16) for training of both parallel beam settings. All of the FBP’s used the Shepp-Logan filter [29].

2) *Cone Beam CT (CBCT) Experiments*: For the CBCT experiments, we used MC-GPU [35], which is a GPU-accelerated X-ray photon transport MC simulation code for CBCT. The code performs the transport simulation in a voxelized geometry and uses CUDA programming supporting multiple GPUs. The code provides access to the total measurement τ_θ , scatter signal s_θ , and primary measurement p_θ for each view θ , eliminating the need to compute p_θ separately.

For training and testing each method in the polychromatic CBCT experiments, we used $\widehat{\mathcal{R}}^{-1}g$ with $g_\theta = -\ln[p_\theta/I_0]$ as the “gold reference” image, and similarly used \tilde{g} , and g^* for the corresponding reconstructions, treating the measurements as in the monochromatic case. Thus, the primary measure-

ment (scatter-free) reconstructions $\widehat{\mathcal{R}^{-1}g}$ include some beam-hardening artifacts, and in our experiments the scatter correction methods do not perform beam-hardening correction, instead focusing on estimating and correcting the scatter.

The geometry for the CBCT experiments is shown in Fig. 5 with a divergent beam point source at source-to-detector distance, $d_{sd} = 180$ cm, and source-to-origin distance, $d_{so} = 130$ cm and with a 64×64 cm² flat panel detector gridded to 128×128 pixels. The source had a 90 keV monoenergetic spectrum for the monochromatic experiments, and the photons were sampled from a 120 keV tungsten spectrum for the polychromatic case.

Again, $\lambda = 5(10^{-2})$ was used for the CBCT setting. For each algorithm, the FDK method [30] with a Shepp-Logan [29] ramp filter was used for reconstructions, with a total of $K = 360$ view angles for each phantom.

The algorithms were compared on two types of phantoms. The first consisted of titanium rods with 2×2 cm² cross-sections placed in parallel with the z-axis with random center locations in the x-y plane sampled from a uniform distribution $\mathcal{U}[-D/4 \text{ cm}, D/4 \text{ cm}]$, where $D = 64$ cm. Intersections between the objects were allowed with intersecting regions also consisting of titanium. The second type of phantoms were used for experiments on medical data. Thirty phantoms extracted from the CT Lymph Nodes dataset [36] from the cancer-imaging archive [37] were tissue-mapped to five different materials and tissue types: (1) air, (2) lung, (3) adipose, (4) soft tissue and (5) bone.

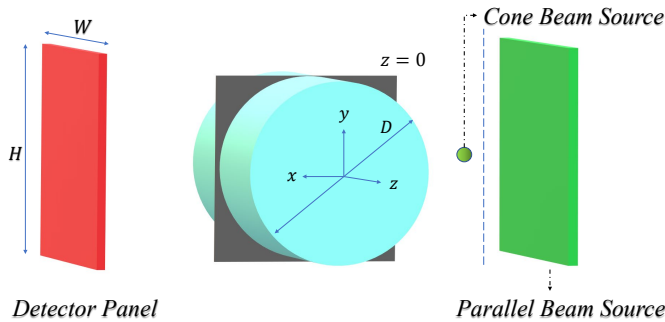


Fig. 5: Imaging geometries for cone and parallel beam CT reconstruction experiments shown together. The gray rectangle at $z = 0$ indicates the central axial 2D slice on the x-y plane.

Since the GPU-accelerated MC code allowed us to simulate photon numbers sufficient to obtain acceptable noise levels in the simulated measurements, a noise reduction scheme as in parallel beam case was not used for CBCT experiments.

B. Setup

The proposed algorithms were compared among themselves and with the recent data-driven projection-based correction method DSE [15], [16] as described in Section I. The DSE method was implemented as described in [15] and trained using the same total measurements τ_θ and primary measurements p_θ used in the training of the proposed methods.

Reconstruction quality, as compared to the reference images (FBP of numerically computed line integrals of test phantoms) is quantified using four metrics: PSNR (in dB) as the ratio of peak reconstruction value to root mean square error; MAE (mean absolute error); PE (peak error), equal to the infinity norm of the error; and SSIM (structural similarity index).

The networks for DSE and the proposed methods were implemented in Pytorch, and the Adam optimizer [32] was used for all methods for training. No additional regularization was used for training, as we observed close validation and training errors, indicating the absence of overfitting.

Computations were performed on an NVIDIA GeForce GTX TITAN X GPU, and an Intel Core i7-4770K CPU with 32 GB RAM. For parallel beam reconstruction, both FBP and image rotations were implemented on the CPU, whereas for CBCT the FDK algorithm was implemented on GPU. The split of run-time averages are shown in Table I. Once both FBPs and image rotations are migrated to the GPU, the DCNN runtimes, which in these experiments account for only a small fraction of the total runtime, will dominate, resulting in total runtimes for the algorithms of 2 – 4 seconds per reconstructed volume.

Algorithm	K	Total	FBP	Rotation	DCNN
PhILSCAT Par-Beam	360	28.2 s	7.7 s	17.9 s	2.6 s
OV-PhILSCAT Par-Beam	180	18.0 s	7.7 s	9.0 s	1.3 s
PhILSCAT CBCT	360	22.6 s	2.1 s	17.9 s	2.6 s

TABLE I: Average run times.

V. EXPERIMENTS

A. Monochromatic 3D Parallel Beam CT

To compare PhILSCAT, OV-PhILSCAT, and DSE [15], [16], each algorithm was trained for 100 epochs and tested on the same 27 and 3 phantoms randomly generated as in Sec. IV-A, respectively. Each phantom had 360 uniformly spaced views with 8×10^6 photons each. For pre-processing, to suppress background noise as described in Sec. IV-A, a 5×5 dilation structuring element and a 2D Gaussian filter with width parameter $\sigma = 2$ were used.

The average and peak scatter-to-primary ratios $s(t, \theta)/p(t, \theta)$ observed in the synthesized projection measurements confirm an expected strong correlation between attenuation along a ray parameterized by (t, θ) and the corresponding scatter-to-primary ratio $s(t, \theta)/p(t, \theta)$. Although overall in the test phantoms, averaged over areas where $p(t, \theta) < I_0$, we observed $\text{AVG}_{t, \theta} s(t, \theta)/p(t, \theta) \approx 7\%$, this ratio increases more than eight-fold to $\text{AVG}_{t, \theta} s(t, \theta)/p(t, \theta) \approx 59\%$ when we average over the areas with $p(t, \theta) < \sqrt{I_0}$. The peak value over all detector pixels for the test phantoms is $\text{max}_{t, \theta} s(t, \theta)/p(t, \theta) = 956\%$.

This shows that the higher values of scatter-to-primary ratio are not restricted to a small number of detector pixels. The strong scatter scenario is also evident in the corruption of the reconstructions from uncorrected total measurements: the peak reconstruction error from the total measurements τ is 1557

HU, which is 46% when normalized by the peak density of 3407 HU of the primary reconstructions from p .

Average reconstruction accuracy metrics are reported in Table II for the three test phantoms. DSE improves on the uncorrected case as expected. However, consistent with our observations, which will be discussed next, PhILSCAT and OV-PhILSCAT perform significantly better than DSE in these experiments on all metrics. OV-PhILSCAT provides not only a slightly better PSNR than PhILSCAT, but is also twice as fast.

	Uncor.	DSE	PhILSCAT	OV-PhILSCAT
PSNR (dB)	38.60	45.35	51.06	51.26
SSIM	0.964	0.984	0.998	0.998
MAE (HU)	19.7	11.3	3.6	3.6
Peak Error (HU)	1572	1228	514	510

TABLE II: Average reconstruction accuracy for three 3D test phantoms for the algorithms. The peak density value of reconstructions using primary measurements p_θ is 3407 HU.

The FBP reconstruction of a test phantom using primary measurements p and the absolute reconstruction errors in HU obtained by the algorithms are shown in Fig. 6, where the display range for the reconstruction is set to $\approx 70\%$ of the maximum value in HU, and that for absolute error is set to $\approx 20\%$ of the reconstruction image. Vertical 1D line profiles extracted from the reconstructions at the same location as in Fig. 6 are compared in Fig. 7.

As expected from the high scatter/primary ratios in the projections, uncorrected reconstructions displaying large magnitude scatter artifacts such as decreased contrast for the axial and sagittal slices, are the worst. DSE corrects these magnitude errors to a significant extent, which is reflected as an overall improvement on the metrics compared to τ -reconstructions. However, as seen in Fig. 6, with DSE there are remaining artifacts around the object edges. Also, DSE does not suppress the streaking artifacts, density errors over highly attenuating objects, and errors in the background very well. This is also seen in the line profile comparisons in Fig. 7.

Both PhILSCAT and OV-PhILSCAT suppress the streaks better than DSE, with better reduction of errors around the object edges, which is especially visible for the titanium slabs in Fig. 6. As a consequence, they both achieve substantially better metrics than DSE. Finally, compared to the total measurement reconstructions, both proposed algorithms reduce the peak error by $\approx 70\%$, whereas DSE by only $\approx 20\%$.

B. 3D Cone Beam CT - Ti Rod Phantoms

In this subsection, we study using both monochromatic and polychromatic sources, a setting more typical of a non-destructive evaluation (NDE) application, with phantoms consisting of randomly placed titanium rods as described in IV-A. These phantoms include high object densities resulting in high ray attenuations. Moreover, the scatter signals corresponding to various views have higher frequency content and there is an increased dependence of the scatter signal on the angle of

the measurement. These factors all have the potential to make the problem more challenging.

DSE and PhILSCAT were each trained on 27 and tested on 3 such phantoms, respectively, using $K = 360$ uniformly spaced views with $P = 10^8$ photons each for each phantom.

As expected with this high density object scenario, the peak scatter-to-primary ratios $s(t, \theta)/p(t, \theta)$ are extremely high due to photon scarcity along highly attenuating paths for both source settings. For the test phantoms, the overall average ratio $\text{AVG}_{t, \theta} s(t, \theta)/p(t, \theta)$, and the corresponding average over areas in the projections where $p_\theta < \sqrt{I_0}$ were found to be 10% and 54%, respectively for the monochromatic case, and 17% and 74%, respectively, for the polychromatic case. These high scatter levels are indicative of difficulty of the reconstruction task in these experiments.

For the monochromatic setting, the observed peak error between the total measurement reconstructions and the true primary reconstructions is 3711 HU, or 42% when normalized by the peak density of 8761 HU in the primary reconstructions. For the polychromatic setting, the corresponding values are 4229 HU or 40% out of the peak primary reconstruction density of 10560 HU. The HU reconstructions for all methods in the polychromatic setting were obtained after performing HU calibration to adjust the water linear attenuation level to 0 HU in the primary measurement reconstructions which were computed as explained in Sec. IV-A.

These numbers indicate a stronger effect of scatter in the reconstructions than in the other CBCT experiments. The average reconstruction accuracy metrics are reported in Tables III and IV, for the monochromatic and polychromatic cases, respectively.

	Uncorrected	DSE	PhILSCAT
PSNR (dB)	35.8	49.8	51.6
SSIM	0.980	0.995	0.997
MAE (HU)	30.1	8.8	8.3
Peak Error (HU)	3327	756	700

TABLE III: Monochromatic CBCT: average reconstruction accuracy for different algorithms for 3 Ti rod test phantoms.

	Uncorrected	DSE	PhILSCAT
PSNR (dB)	36.84	49.66	50.86
SSIM	0.988	0.996	0.997
MAE (HU)	35.0	15.1	15.1
Peak Error (HU)	4229	1885	1111

TABLE IV: Polychromatic CBCT: average reconstruction accuracy for different algorithms for 3 Ti rod test phantoms.

Reference reconstructions computed using primary measurements p , scatter corrected reconstructions, and error magnitude plots are given in Figures 8 and 9, for the monochromatic and polychromatic cases, respectively.

To facilitate comparison, line profiles for each method and maximum intensity projections (MIP) of the error volumes

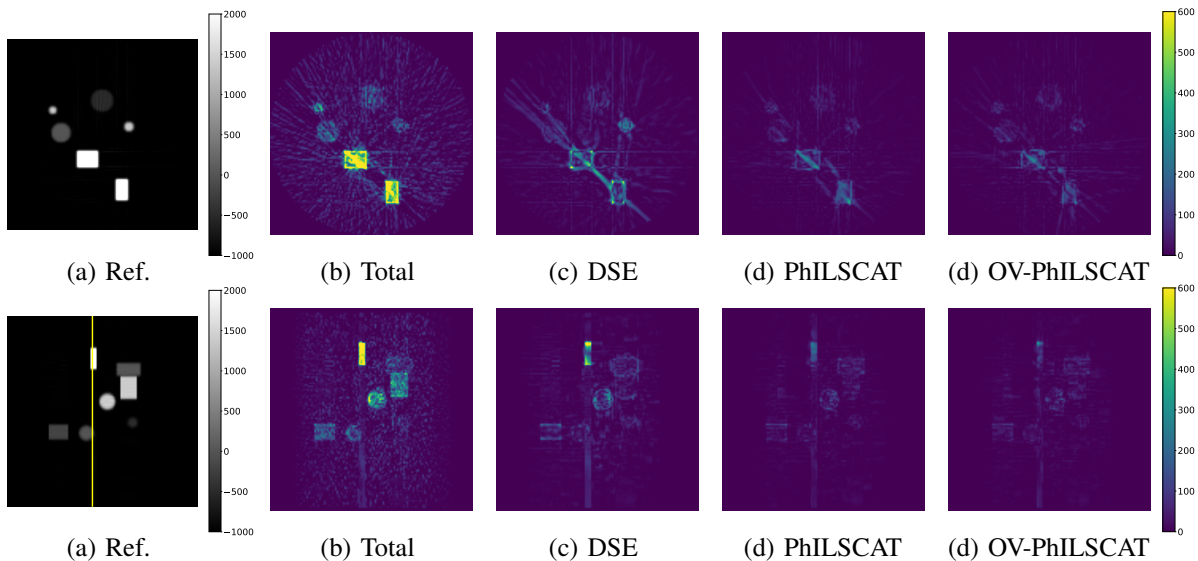


Fig. 6: Monochromatic parallel-beam reconstructions – an axial & a sagittal slice: reconstruction using primary measurements, p_θ in (a)&(f); magnitude of the error using total measurements τ in (b)&(g), vs. using primary measurements p_θ^* estimated by DSE in (c)&(h), by PhILSCAT. in (d)&(i), and by OV-PhILSCAT in (e)&(j).

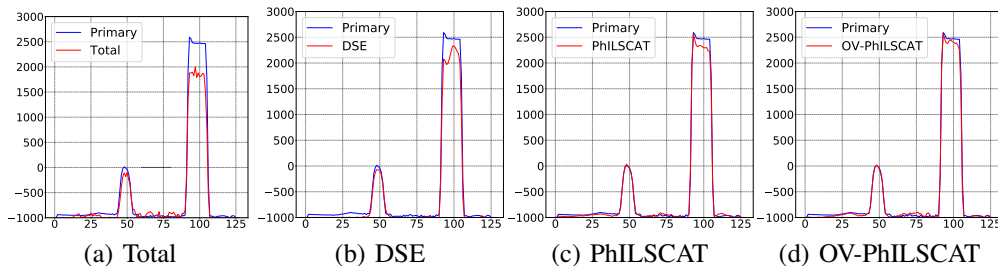


Fig. 7: Monochromatic parallel-beam reconstructions: vertical line profiles from Fig. 6 (f). Comparisons between using total measurements τ in (a), vs. primary measurements p_θ^* estimated by DSE in (b), PhILSCAT in (c), and OV-PhILSCAT in (d).

for DSE and PhILSCAT are provided together in Figures 9 and 10 for the polychromatic case. An MIP in a particular direction is obtained by assigning to the projection the maximum absolute values the rays encounter in any voxel they traverse. As could be expected from the strong scatter, the total measurement reconstructions contain large magnitude errors ranging between 1000 HU and 2000 HU over the objects. The projection-domain DSE algorithm improves considerably on these magnitude errors. However, there still remain relatively large errors on the highly attenuating paths. PhILSCAT corrects scatter related artifacts noticeably better over those regions while not suffering any setbacks on any other part of the reconstruction compared to DSE. Additionally, streaking artifacts are suppressed to a greater extent using PhILSCAT. Thanks to these differences, PhILSCAT performs better than DSE in terms of PSNR, SSIM and the peak error, as revealed by the metrics reported in Tables III and IV.

C. Polychromatic CBCT - Anthropomorphic Phantoms

For the polychromatic 3D CBCT reconstructions, DSE and PhILSCAT were each trained on 27 and tested on 3 anthropomorphic phantoms as described in Section IV-A with the imaging geometry shown in Fig. 5.

The peak error between the total measurement reconstruc-

tions of the three test phantoms and the true primary reconstructions was 1699 HU, or 84% when normalized by the peak density of 2034 HU in the primary reconstructions, indicating significant degradation due to uncorrected scatter.

The average and the peak scatter-to-primary ratios for the three test phantoms were $\text{AVG}_{t,\theta} s(t,\theta)/p(t,\theta) = 29\%$, and $\text{max}_{t,\theta} s(t,\theta)/p(t,\theta) = 212\%$, with $\text{AVG}_{t,\theta} s(t,\theta)/p(t,\theta) = 79\%$ over areas in the projections where $p(t,\theta) < \sqrt{I_0}$. The closer scatter-to-primary ratios in areas with $p(t,\theta) < I_0$ vs. those with $p(t,\theta) < \sqrt{I_0}$ indicate that the scatter signals tend to be smoother for these phantoms compared to the Ti rod experiments in Section V-B. Owing to this characteristic, the difference in reconstruction quality between PhILSCAT and DSE, as expressed by the average PSNR and SSIM results for the 3 test phantoms in Table V, is reduced compared to Sec. V-B. Still, PhILSCAT suppresses the peak error 20% better than DSE, and does better in terms of PSNR and MAE on average.

Consistent with the results of other experiments, as seen in the comparison of the magnitude of the reconstruction errors in Fig. 11, PhILSCAT performs visibly better than DSE, especially in highly attenuating regions of the phantoms.

VI. CONCLUSIONS

We proposed two novel physics-inspired deep learning-based algorithms for scatter correction in X-ray CT images.

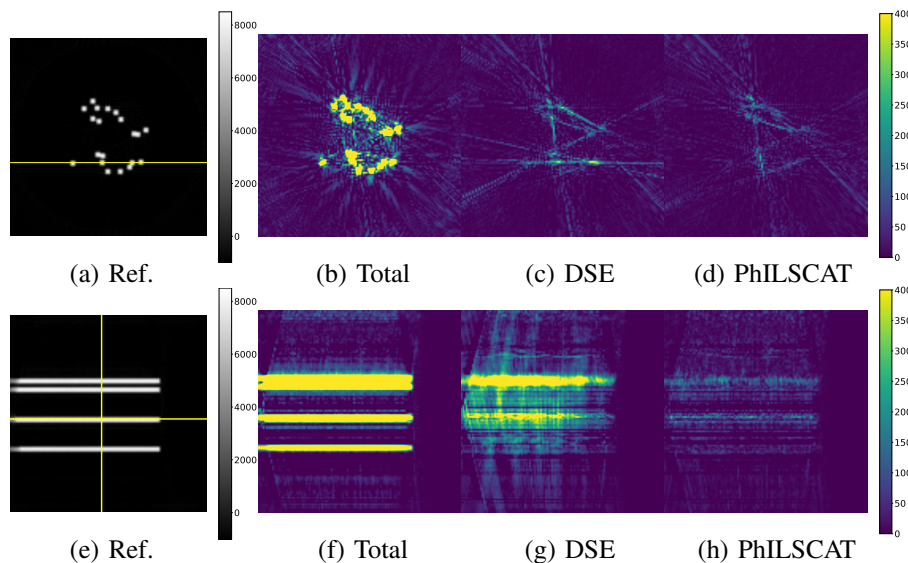


Fig. 8: Monochromatic CBCT reconstructions of Ti rod test phantom. Numerical values in HU. Central axial slice & sagittal slice: reconstruction using primary measurements p in (a)&(e); magnitude of the error using total measurements τ_θ in (b)&(f); vs. using primary measurements p^* estimated by DSE in (c)&(g); and by PhILSCAT in (d)&(h).

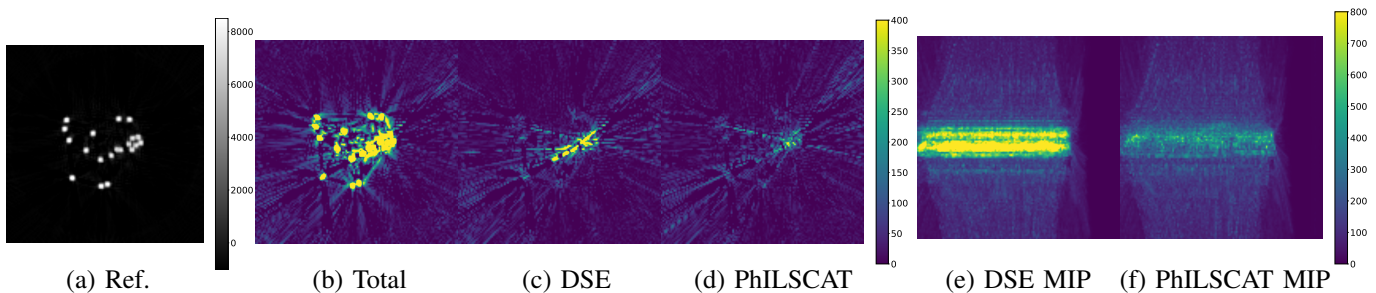


Fig. 9: Polychromatic CBCT reconstruction of Ti rod test phantom – central axial slice. Numerical values in HU. Reconstruction using primary measurements, p in (a); magnitude of the error using total measurements τ in (b), vs. using primary measurements p^* estimated by DSE in (c), and by PhILSCAT in (d). Sagittal slice maximum intensity projections (MIP) of the error volumes: using p^* estimated by DSE in (e), and by PhILSCAT in (f).

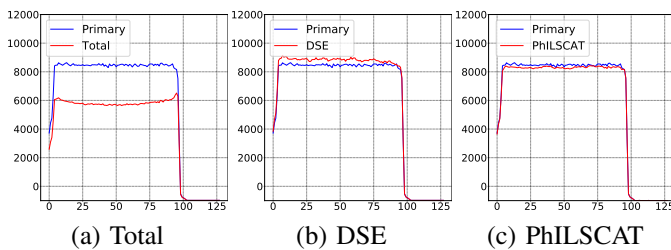


Fig. 10: Polychromatic CBCT reconstructions of Ti rod test phantom: horizontal line profiles indicated in Fig. 9: (a) Using total measurements τ_θ ; vs. using primary measurements p_θ^* estimated by (b) DSE; and (c) by PhILSCAT.

The empirical results for the proposed methods demonstrate their advantage in various settings to another recent projection-by-projection-based data-driven de-scattering method. The proposed algorithms use scatter-corrupted measurements and an initial reconstruction of the object obtained from these measurements to estimate and correct the scatter in the projection domain. Unlike previous data-driven methods, the proposed algorithms incorporate constraints that are motivated by the

	Uncorrected	DSE	PhILSCAT
PSNR (dB)	26.85	36.81	37.15
SSIM	0.86	0.975	0.975
MAE (HU)	35.8	12.9	12.3
Peak Error (HU)	1699	970	800

TABLE V: Polychromatic CBCT reconstructions of anthropomorphic phantoms: average reconstruction accuracy results for 3 test phantoms.

physics of the CT imaging. The cost function for training the algorithms is tailored to be able to express the norm of an image-domain error in the projection domain, but without the need for using the filtered backprojection.

Possible directions for future work can be further investigation of the spectral properties of scatter signals to improve de-scattering algorithms, and theoretical analysis of the factors limiting the performance of such learning-based algorithms.

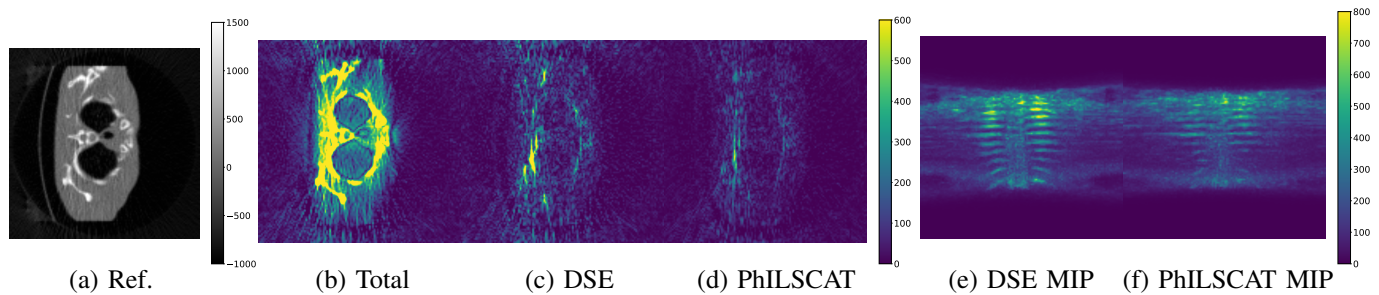


Fig. 11: Polychromatic CBCT reconstructions of an anthropomorphic test phantom - axial slice. Numerical values in HU. (a) Reconstruction using primary measurements, p_θ ; magnitude of the error (b) using total measurements τ ; vs. using primary measurements p^* estimated by (c) DSE; and (d) by PhILSCAT. Coronal slice maximum intensity projections (MIP) of the error volumes: using p^* estimated by DSE in (e), and by PhILSCAT in (f).

REFERENCES

- [1] C. L. Epstein, *Introduction to the Mathematics of Medical Imaging*, 2nd ed., C. L. Epstein, Ed. Philadelphia, PA: Society for Industrial and Applied Mathematics, 2007. [Online]. Available: <https://epubs.siam.org/doi/abs/10.1137/9780898717792>
- [2] C. Floyd, R. Jaszczak, C. Harris, and R. Coleman, "Energy and spatial distribution of multiple order Compton scatter in SPECT: A Monte Carlo investigation," *Phys. Med. Biol.*, vol. 29, no. 10, p. 1217, 1984.
- [3] E.-P. Rührschopf and K. Klingenberg, "A general framework and review of scatter correction methods in x-ray cone-beam computerized tomography. Part I: Scatter compensation approaches," *Med. Phys.*, vol. 38, no. 7, pp. 4296–4311, 2011.
- [4] G. Poludniowski, P. Evans, V. Hansen, and S. Webb, "An efficient monte carlo-based algorithm for scatter correction in kev cone-beam ct," *Phys. Med. Biol.*, vol. 54, no. 12, p. 3847, 2009.
- [5] A. Maslowski *et al.*, "Acuros CTS: A fast, linear Boltzmann transport equation solver for computed tomography scatter—Part I: Core algorithms and validation," *Med. Phys.*, vol. 45, no. 5, 2018.
- [6] A. Shiroma *et al.*, "Scatter correction for industrial cone-beam computed tomography (CBCT) using 3D VSHARP, a fast GPU-Based linear Boltzmann transport equation solver," *9th Conference on Industrial Computed Tomography (iCT)*, 2019.
- [7] C. Bai, G. L. Zeng, and G. T. Gullberg, "A slice-by-slice blurring model and kernel evaluation using the Klein-Nishina formula for 3D scatter compensation in parallel and converging beam spect," *Phys. Med. Biol.*, vol. 45, no. 5, 2000.
- [8] O. Klein and Y. Nishina, "Über die Streuung von Strahlung durch freie Elektronen nach der neuen relativistischen Quantendynamik von Dirac," *Zeitschrift für Physik*, vol. 52, no. 11-12, 1929.
- [9] B. Ohnesorge, T. Flohr, and K. Klingenberg-Regn, "Efficient object scatter correction algorithm for third and fourth generation CT scanners," *Eur. Radiol.*, vol. 9, no. 3, 1999.
- [10] W. Zhao *et al.*, "Patient-specific scatter correction for flat-panel detector-based cone-beam CT imaging," *Phys. Med. Biol.*, vol. 60, no. 3, 2015.
- [11] J. Star-Lack *et al.*, "Efficient scatter correction using asymmetric kernels," in *Med. Imaging 2009: Phys. of Med. Imaging*, vol. 7258. International Society for Optics and Photonics, 2009.
- [12] S. Xie *et al.*, "Scatter artifacts removal using learning-based method for CBCT in IGRT system," *IEEE Access*, vol. 6, 2018.
- [13] L. Shi *et al.*, "Library based x-ray scatter correction for dedicated cone beam breast CT," *Med. Phys.*, vol. 43, no. 8, 2016.
- [14] H. Lee and J. Lee, "A deep learning-based scatter correction of simulated X-ray images," *Electronics*, vol. 8, no. 9, 2019.
- [15] J. Maier *et al.*, "Deep Scatter Estimation (DSE): Accurate real-time scatter estimation for X-ray CT using a deep convolutional neural network," *Jour. of Nondest. Eval.*, vol. 37, no. 3, p. 57, 2018.
- [16] J. Maier, E. Eulig, T. Vöth, M. Knaup, J. Kuntz, S. Sawall, and M. Kachelrieß, "Real-time scatter estimation for medical CT using the deep scatter estimation: Method and robustness analysis with respect to different anatomies, dose levels, tube voltages, and data truncation," *Med. Phys.*, vol. 46, no. 1, pp. 238–249, 2019.
- [17] O. Ronneberger, P. Fischer, and T. Brox, "U-net: Convolutional networks for biomedical image segmentation," in *Med. Image Comp. & Comp.-Assist. Interv.*, vol. 9351. Springer, 2015.
- [18] B. Iskender and Y. Bresler, "A physics-motivated DNN for X-ray CT scatter correction," in *2020 IEEE 17th International Symposium on Biomedical Imaging (ISBI)*, 2020, pp. 609–613.
- [19] B. Iskender and Y. Bresler, "X-ray CT scatter correction by a physics-motivated DNN with opposite view processing," in *The 6th International Conference on Image Formation in X-Ray Computed Tomography (CT Meeting)*, 2020, pp. 308–311.
- [20] Y. Hwu, G. Margaritondo, and A.-S. Chiang, "Q&a: Why use synchrotron x-ray tomography for multi-scale connectome mapping?" *BMC biology*, vol. 15, no. 1, pp. 1–9, 2017.
- [21] E. Newham, I. J. Corfe, K. R. Brown, N. Gostling, P. Gill, and P. Schneider, "Synchrotron radiation-based x-ray tomography reveals life history in primate cementum incrementation," *J. R. Soc. Interface*, vol. 17, 2020.
- [22] R. Baba, A. Yoneyama, K. Hyodo, T. Takeda, M. Takahashi, H. Nakano, and K. Maki, "Improving image quality of synchrotron ct by scattered x-ray correction," in *J. Phys. Conf. Ser.*, vol. 425, no. 19, 2013, p. 2010.
- [23] M. Voltolini, A. Haboub, S. Dou, T.-H. Kwon, A. A. MacDowell, D. Y. Parkinson, and J. Ajo-Franklin, "The emerging role of 4d synchrotron x-ray micro-tomography for climate and fossil energy studies: five experiments showing the present capabilities at beamline 8.3. 2 at the advanced light source," *J. Synchrotron Radiat.*, vol. 24, no. 6, pp. 1237–1249, 2017.
- [24] B. Hornberger, J. Kasahara, M. Gifford, R. Ruth, and R. Loewen, "A compact light source providing high-flux, quasi-monochromatic, tunable x-rays in the laboratory," in *Advances in Laboratory-based X-Ray Sources, Optics, and Applications VII*, vol. 11110. International Society for Optics and Photonics, 2019, p. 1111003.
- [25] A. Bazzani, P. Cardarelli, G. Paternò, M. Placidi, A. Taibi, and G. Turchetti, "Bocxs: A compact multidisciplinary x-ray source," *Physics Open*, vol. 5, p. 100036, 2020.
- [26] W. Huda and R. Slone, *Review of Radiologic Physics*, ser. High-Yield Systems Series. Lippincott Williams & Wilkins, 2003. [Online]. Available: <https://books.google.com/books?id=ksH6aUYqqawC>
- [27] Beer, "Bestimmung der absorption des rothen lichts in farbigen flüssigkeiten," *Annalen der Physik*, vol. 162, no. 5, pp. 78–88, 1852. [Online]. Available: <https://onlinelibrary.wiley.com/doi/abs/10.1002/andp.18521620505>
- [28] J. Bushberg, J. Seibert, E. Leidholdt, and J. Boone, *The Essential Physics of Medical Imaging*. Wolters Kluwer Health, 2011. [Online]. Available: <https://books.google.com/books?id=RKcTgTqeniwC>
- [29] L. A. Shepp and B. F. Logan, "The fourier reconstruction of a head section," *IEEE Trans. Nucl. Sci.*, vol. 21, no. 3, pp. 21–43, 1974.
- [30] L. A. Feldkamp, L. C. Davis, and J. W. Kress, "Practical cone-beam algorithm," *Josa a*, vol. 1, no. 6, pp. 612–619, 1984.
- [31] A. Paszke, S. Gross, S. Chintala, G. Chanan, E. Yang, Z. DeVito, Z. Lin, A. Desmaison, L. Antiga, and A. Lerer, "Automatic differentiation in pytorch," in *NIPS-W*, 2017.
- [32] D. P. Kingma and J. Ba, "Adam: A method for stochastic optimization," *arXiv preprint arXiv:1412.6980*, 2014.
- [33] S. Jan *et al.*, "Gate: a simulation toolkit for PET and SPECT," *Phys. Med. Biol.*, vol. 49, no. 19, 2004.
- [34] S. Agostinelli *et al.*, "Geant4— a simulation toolkit," *Nucl. Instrum. Methods Phys. Res.*, vol. 506, no. 3, 2003.
- [35] A. Badal and A. Badano, "Accelerating Monte Carlo simulations of photon transport in a voxelized geometry using a massively parallel

- graphics processing unit," *Med. Phys.*, vol. 36, no. 11, pp. 4878–4880, 2009.
- [36] H. R. Roth, L. Lu, A. Seff, K. M. Cherry, J. Hoffman, S. Wang, J. Liu, E. Turkbey, and R. M. Summers, "A new 2.5 D representation for lymph node detection using random sets of deep convolutional neural network observations," in *Intl. Conf. on Med. Image Comp. & Comp.-Assist. Interv.* Springer, 2014, pp. 520–527.
- [37] K. Clark, B. Vendt, K. Smith, J. Freymann, J. Kirby, P. Koppel, S. Moore, S. Phillips, D. Maffitt, M. Pringle *et al.*, "The Cancer Imaging Archive (TCIA): Maintaining and operating a public information repository," *J. Digit. Imaging*, vol. 26, no. 6, pp. 1045–1057, 2013.